

Force-Dependent Regulation of Talin–KANK1 Complex at Focal Adhesions

Miao Yu,^{†,‡} Shimin Le,^{‡,§} York-Christoph Ammon,^{§,#} Benjamin T. Goult,^{||} Anna Akhmanova,^{*,§} and Jie Yan^{*,†,‡,⊥}

[†]Mechanobiology Institute, National University of Singapore, Singapore

[‡]Department of Physics, National University of Singapore, Singapore

[§]Cell Biology, Department of Biology, Faculty of Science, Utrecht University, Utrecht, The Netherlands

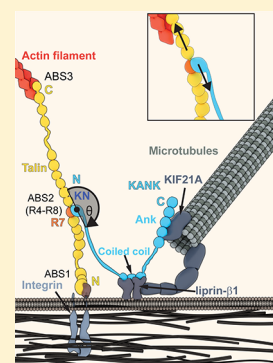
^{||}School of Biosciences, University of Kent, Canterbury, United Kingdom

[⊥]Centre for Bioimaging Sciences, National University of Singapore, Singapore

Supporting Information

ABSTRACT: KANK proteins mediate cross-talk between dynamic microtubules and integrin-based adhesions to the extracellular matrix. KANKs interact with the integrin/actin-binding protein talin and with several components of microtubule-stabilizing cortical complexes. Because of actomyosin contractility, the talin–KANK complex is likely under mechanical force, and its mechanical stability is expected to be a critical determinant of KANK recruitment to focal adhesions. Here, we quantified the lifetime of the complex of the talin rod domain R7 and the KN domain of KANK1 under shear-force geometry and found that it can withstand forces for seconds to minutes over a physiological force range up to 10 pN. Complex stability measurements combined with cell biological experiments suggest that shear-force stretching promotes KANK1 localization to the periphery of focal adhesions. These results indicate that the talin–KANK1 complex is mechanically strong, enabling it to support the cross-talk between microtubule and actin cytoskeleton at focal adhesions.

KEYWORDS: KANK1, talin, focal adhesions, mechanotransduction, magnetic tweezers



INTRODUCTION

Integrin-based adhesions (focal adhesions, FAs) are large macromolecular assemblies, which are crucial for cell migration, growth, and proliferation, as well as tissue formation and maintenance, because they transmit mechanical force and regulatory signals between cells and the extracellular matrix (ECM).^{1,2} The molecular architecture of FAs is built up by a set of proteins including talin, paxillin, vinculin, and filamentous actin.³ FAs are dynamic assemblies of these proteins that assemble on the cytoplasmic face of the integrin, and their life cycle is regulated by the coordinated actions of both actomyosin and the microtubule (MT) cytoskeleton.⁴ MTs interact with FAs through a network of scaffolding proteins, among which the evolutionarily conserved KANK family proteins play a crucial role.⁵

The KANK family of proteins (KANK1–KANK4) are characterized by their unique structure, with the family specific KN motif at the N-terminus, followed by coiled-coil domains and ankyrin-repeats (Ank domain) in the C-terminal region⁶ (see Figure 1a, left panel). The KN motif consists of 22–23 residues and is highly conserved across the KANK family.⁷ KANK proteins interact with the cortical MT stabilization complexes (CMSCs) by binding to liprin-β1 through their coiled-coil domain. Moreover, KANK1 recruits KIF21A to CMSCs through the Ank domain.^{8,9} By interacting with talin

through the KN domain, KANK1 and KANK2 recruit to the peripheral zone of FA (“FA belt”) the scaffolding protein liprin-β1, which tethers additional CMSC components and connect the MT targeting machinery to integrins.^{7,10} Through these interactions, KANK proteins mediate a cross-talk between actin cytoskeleton and microtubule cytoskeleton networks at FAs.^{5,7,10,11}

Talin is a mechanosensitive protein that links the integrin-mediated cell-matrix contacts to the actin cytoskeleton. Talin comprises an N-terminal FERM domain that binds to the cytoplasmic tails of integrins and a C-terminal rod domain containing 13 α-helical bundles (R1–R13) terminating with a single α-helix that mediates talin dimerization.¹² It also contains three actin binding sites located at the C-terminal end (ABS3),¹³ four consecutive α-helical bundles in the rod (R4–R8, ABS2),^{12,14,15} and an additional binding site located at the N-terminus (ABS1).¹⁶ Both talin isoforms, talin1 and talin2, were shown to interact with KANK1 and KANK2 through the KN-domain, which is an α-helix containing a leucine-aspartic acid (LD) motif.¹⁷ The KN-domain interacts with the talin R7 domain via the “helix-addition” binding

Received: April 27, 2019

Revised: August 7, 2019

Published: August 7, 2019

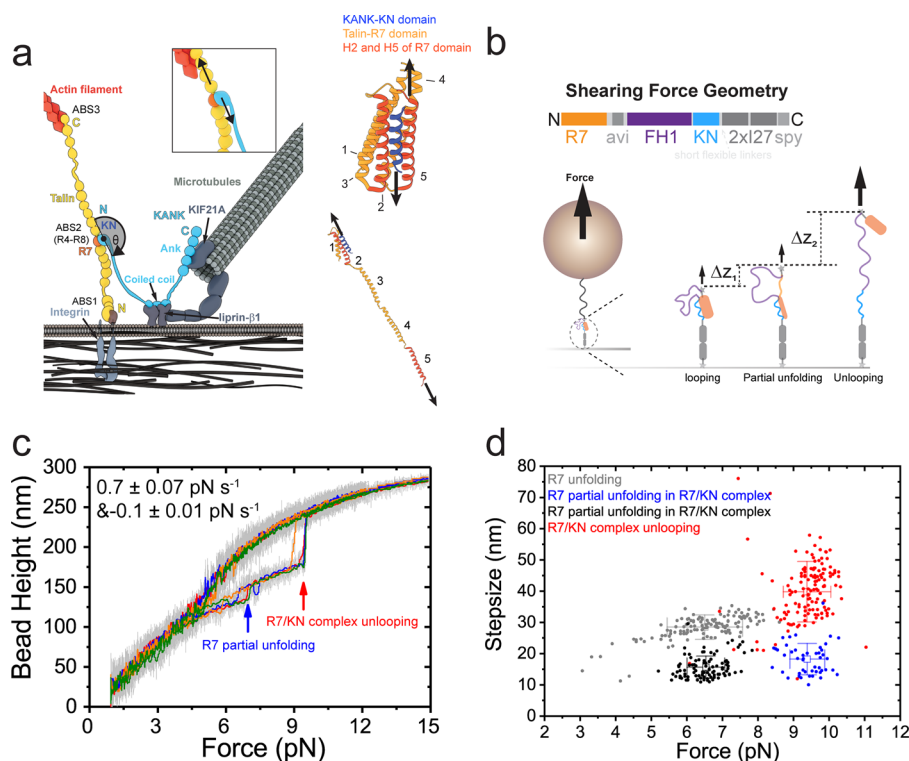


Figure 1. Mechanical stability of the R7/KN complex. (a) Illustration of the talin and KANK interaction at FAs. Left panel shows the FA core of integrin coupled to the actin cytoskeleton via talin. KANK (blue) mediates the linkage between talin and the CMSC (indicated liprin- β 1, a component of CMSC), which binds to MTs. (Inset shows the geometry of the forces acting on the talin-R7:KANK-KN interaction.) Right panel shows the structural model of the R7/KN complex under shear-force geometry with R7 domain folded (top) and R7 domain partially unfolded (bottom) in the complex. (b) Top panel shows a single-molecule detector construct of R7/KN complex (N-to-C terminus): R7 domain, avi-tag, FH1 linker, KANK1-KN domain, two I27 domains, and spy-tag. Bottom panel shows that the force is applied through the C-termini of KANK1-KN and Talin1-R7. The R7/KN complex formed at low forces can be unlooped at increased force, and R7/KN complex partially unfolding can occur before unlooping. The difference in bead height between the paired-looped state and the partially unfolded state is indicated by Δz_1 , and that between partially unfolded state and the unpaired-unlooped state is indicated by Δz_2 . (c) Four representative color-indicated force–extension curves of the single-molecule detector at force loading rates of $0.70 \pm 0.07 \text{ pN s}^{-1}$ (force increase) and $-0.1 \pm 0.01 \text{ pN s}^{-1}$ (force decrease). The large extension jumps (red arrow) at $\sim 9 \text{ pN}$ correspond to unlooping of the R7/KN complex; the smaller extension jumps (blue arrow) at $6\text{--}7 \text{ pN}$ correspond to partial unfolding of the R7 domain in the R7/KN complex. (d) The force–step size graph of the two extension jumps of R7/KN complex during force increase ($\sim 0.7 \text{ pN s}^{-1}$), which reveals three distinct groups, indicated by the colors red, blue, and black. The red data points represent R7/KN complex unlooping, with a force of $9.4 \pm 0.7 \text{ pN}$ (mean \pm standard deviation) and step size of $39.8 \pm 9.7 \text{ nm}$. The black and blue data points represent the partial unfolding of talin1-R7 domain in the R7/KN complex with force of $6.5 \pm 0.5 \text{ pN}$ and step size of $15.6 \pm 3.6 \text{ nm}$ (black) and of $9.4 \pm 0.5 \text{ pN}$ and of $18.2 \pm 5.0 \text{ nm}$ (blue), respectively. Data obtained for single R7 domain unfolding during force increase (gray data points, $\sim 0.5 \text{ pN s}^{-1}$) are provided for comparison, with a force of $6.5 \pm 1.1 \text{ pN}$ and a step size of $28.5 \pm 3.9 \text{ nm}$. Over 100 data points were obtained from at least five independent tethers for R7 partial unfolding, R7/KN complex unlooping, and single R7 domain unfolding. The error bars in the graph indicate the mean value and standard deviation of the data in each group.

mode, whereby the KANK KN-domain packs against the side of the 5-helix R7 bundle (see Figure 1a, right panel).^{7,10,18} KANK1/2 binding to talin R7 can interfere with the actin binding to ABS2.¹⁰

The talin-R7/KANK-KN (R7/KN) complex is likely subject to mechanical force due to actomyosin contractility that generates a pulling force on talin.^{15,19} The F-actin binding through ABS3 subjects all the domains in the talin rod to mechanical stretching.²⁰ As talin is tethered to the integrin at the plasma membrane, the mechanical deformation of talin under tensile force is expected to increase the distance between R7 and the membrane, which, in turn, would result in mechanical stretching of the region of KANK1/2 between the cortex-associated coiled coil domain and the talin R7-associated KN domain (Figure 1a).

The crucial role of KANK1/2–talin interaction in KANK's functions implies that the R7/KN complex should be able to withstand physiological levels of forces. It has been shown that

the forces in talin-mediated force transmission pathways are typically on the order of a few piconewtons (pN).^{21–24} The lifetime of talin in FAs was estimated using fluorescence recovery after photobleaching (FRAP) assay in the order of a few tens of seconds.^{25,26} Based on this information, we hypothesized that the R7/KN complex can withstand forces of a few piconewtons over a time scale on the order of seconds to minutes.

In cells, the force applied to the R7/KN complex is through the C-termini of R7 and KN (Figure 1a). Depending on the distance between the talin–FERM associated with integrin at the membrane and the KANK-coiled coil domain associated with the CMSC complex on membrane, and the angle of the talin rod relative to the two, the force on talin R7 and that on KANK-KN can have an angle in the range of $90^\circ \leq \theta \leq 180^\circ$ (Figure 1a). The two extremes correspond to shear-force geometry ($\theta = 180^\circ$) and unzip-force geometry ($\theta = 90^\circ$), which are known to correspond to the strongest and weakest

mechanical stabilities of a molecular complex, respectively.^{27–29} We reasoned that the more mechanically stable R7/KN complex under shear force predominates the talin–KANK linkage. In this work, we used magnetic tweezers^{30,31} to investigate the mechanical stability of R7/KN complex under the shear-force geometry (see Figure 1a, right (top panel) and Figure 1b). Furthermore, we performed cell biological experiments to test whether shear-force stretching geometry can promote KANK1 localization to the periphery of FAs. Our results suggest that the talin–KANK1 complex is mechanically strong, enabling it to support the cross-talk between microtubule and actin cytoskeleton at FAs, and shear-force stretching can promote KANK1 localization to the FA belt.

RESULTS

R7/KN Complex Can Resist Piconewton-Range Shear Force. Measuring biomolecular interactions under mechanical force with magnetic tweezers is complicated by the presence of two molecules. One strategy to study such interactions is to tether the superparamagnetic bead on one molecule (e.g., the KN domain), which would bind to the other molecule (e.g., talin R7) tethered to the surface. In this scenario, force exerted on the bead is transmitted to the interaction interface. However, after a single force extension cycle, the tether would be lost due to dissociation of the complex. A meaningful experiment would thus require stretching of many independent tethers, which makes it difficult to perform experiments with high throughput.

To enable precise direct quantification of molecular complexes under the shear-force geometry (Figure 1a, right (top panel)), we performed the experiments using a novel single-molecule detector. The detector was comprised of an R7 domain of talin1 and a KN domain of KANK1, connected by a long flexible linker (222 a.a.), mainly derived from the FH1 domain of Diaph1, which we have characterized previously³² (see Figure 1b). We also included two well-characterized titin I27 domains in the detector, which serve as a molecular spacer between the target R7/KN complex and the surface (Figure 1b). An avi-tag is inserted near the C-terminus of the R7 domain, and a spy-tag is attached at the C-terminus of the second I27 domain (Figure 1b). In addition, each domain is surrounded by short flexible linkers of several residues to ensure the flexibility of the detector. The detector was tethered between a coverslip and a 572-bp DNA handle linked 2.8- μ m-diameter superparamagnetic bead (the DNA handle serves as a molecular spacer between the complex and the bead), and was stretched by forces applied using magnetic tweezers that were made in-house.^{30,31,33} In this design, after the R7/KN complex dissociates, the tether promotes complex reformation after force is released. Thus, one tether can be reused multiple times, which increases the throughput of the experiments. The detector has two conformational states: a *looped* state, where R7 and KN form a complex, and an *unlooped* state, where the R7 and KN are separated. Because of the long flexible linker, when subjected to force, the two states have significant differences in extension. The height of the bead in the longer unlooped state is higher than that in the shorter looped state, and this difference can be detected by the setup in real time at a nanometer spatial resolution for the bead height.³⁰

Using this experimental setup, we obtained the force-dependent time traces of the bead height change. Figure 1c shows representative force-bead height curves during four consecutive cycles of force-increase (loading rate of 0.7 ± 0.07

pN s⁻¹) and force-decrease (loading rate of -0.1 ± 0.01 pN s⁻¹) scans (indicated by different colors) of a single tether. Two stepwise extension increases were observed during the force-increase scan: one at ~ 6.5 pN, with a step size of ~ 15 nm (blue arrow), and the other at ~ 9.5 pN, with a step size of ~ 40 nm (red arrow). Since the KN domain is an unstructured peptide and R7 is not under force if the R7/KN complex is disengaged (Figure 1b), it is unlikely to have unlooping in the first step and unfolding in the second step. Therefore, we can assign the first stepwise extension increase to be partial unfolding of the R7/KN complex and the second step can be assigned to be complete rupture of the complex, which results in unlooping of the detector. The complex could also be ruptured in a one-step process with a larger step size (see Figure S1 in the Supporting Information), which can be explained by concurrent partial unfolding and unlooping, or direct unlooping without partial unfolding of the complex.

Figure 1d shows the force-step size graph of the transition events obtained. The data suggest that the partial unfolding in the two-step process could occur at two distinct mechanical stability groups (black and blue), indicated by the well-separated unfolding forces at 6.5 ± 0.5 pN (mean \pm standard deviation) and at 9.4 ± 0.5 pN, respectively. For comparison, unfolding of R7 alone occurs at forces of $\sim 6.5 \pm 1.1$ pN with a step size of 28.5 ± 3.9 nm (Figure 1d, gray). The presence of two mechanically stable groups of partial unfolding of talin R7 in the R7/KN complex likely indicates the presence of two transition pathways with different force-dependent kinetics. Despite the different transition forces, the two groups of partial unfolding have very similar transition step sizes of 15.6 ± 3.6 nm and 18.2 ± 5.0 nm. Such step sizes are much shorter than the extension change expected from dissociation of the R7/KN complex, which is consistent with the explanation that they correspond to partial unfolding of the R7/KN complex. Fitting the partial-unfolding force distributions for the black and blue groups with Bell's model^{34,35} reveals large transition distances of 6–8 nm associated with partial unfolding of the R7/KN complex (see Figures S2 and S3 in the Supporting Information), suggesting large conformational changes of the R7/KN complex preceding the partial unfolding transitions.

The red group, which is characterized with a large step size of 39.8 ± 9.7 nm and a transition force of 9.4 ± 0.7 pN, represents the complete rupture of the R7/KN complex. Data in this group include the second stepwise extension increases in the two-step process and the stepwise extension increases in the single-step process. Direct unlooping without partial unfolding is expected to be associated with a step size of ~ 55 nm at ~ 10 pN, because of the presence of the long flexible linker and based on worm-like-chain (WLC) model estimation (see Supplementary Text S2 in the Supporting Information).^{32,36,37} In contrast, if partial unfolding precedes the final rupturing of the complex, the extension of the linker is pre-extended (Figure 1b). As a result, the step size associated with the final rupturing of the complex can be significantly less. This explains why the step sizes of the unlooping spread over a range from 15 nm to 55 nm (Figure 1d, red). Similar to the partial unfolding transition, a large transition distance of ~ 8 nm was estimated for the unlooping transition based on Bell's model fitting, suggesting a large conformational change of the R7/KN complex preceding the final rupture of the complex (see Figure S2 in the Supporting Information).

R7/KN Complex Exhibits Catch-to-Slip Bond Switching Behavior. In order to quantify the mechanical stability of

the R7/KN complex, we measured the lifetime of the R7/KN complex at different forces using a force-jump-cycle procedure by holding the R7/KN complex at different forces and recording the dwell time until the unlooping transition occurred. Briefly, in each force-jump cycle, the molecule was first held at a low force of ~ 2 pN for ~ 10 s (blue data in Figure 2a) to allow the formation of the R7/KN complex, and then

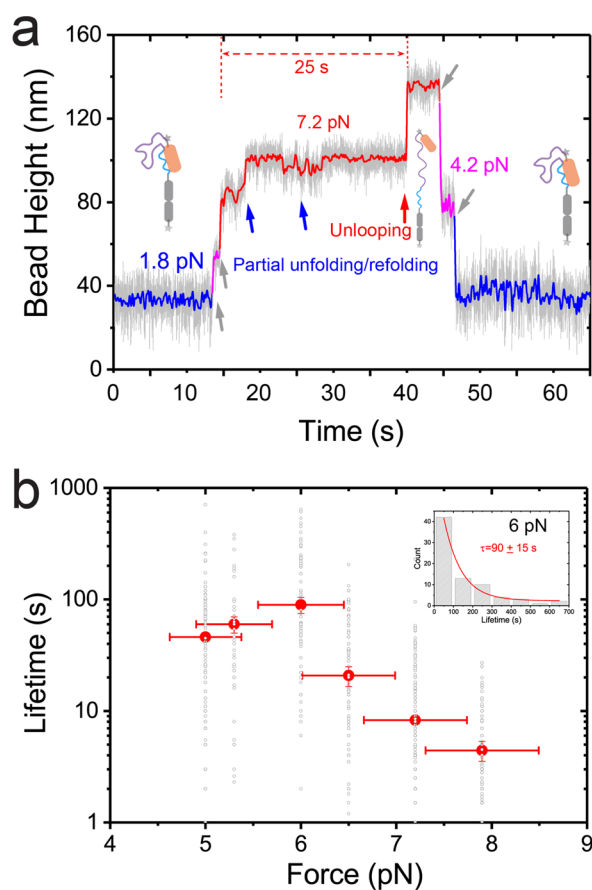


Figure 2. Mechanical lifetime of the R7/KN complex. (a) Representative time trace of extension change during force-jumping assay to quantify the mechanical lifetime of the R7/KN complex at various forces. In such an assay, after jumping from 1.8 pN to a higher force, the average lifetime of the complex at the higher force is measured in multiple cycles. In this example, the lifetime (~ 25 s, indicated by dashed red arrow) of the complex at 7.2 pN in one force jump is shown. Blue arrows indicate stepwise extension changes associated with partial unfolding/refolding prior to unlooping. The red arrow indicates stepwise extension change associated with unlooping. The gray arrows indicate force change-induced bead height changes during force jumps. The insets show the sketches of the detector in the looped state at ~ 1.8 pN and the unlooped state at ~ 7.2 pN. Additional examples of time trace extension change during force-jumping assay are shown in Figure S4 in the Supporting Information. (b) Force-dependent lifetime of the R7/KN complex. The hollow gray circles represent each individual lifetime measured. The red solid circles represent the characteristic lifetime obtained from exponential decay fitting of the raw data at each force. Inset shows a representative exponential fitting for data obtained at 6 pN, the exponential decay fitting of the lifetime distributions at all forces are shown in Figure S5 in the Supporting Information. The lateral-error bar indicates 10% force calibration error of the magnetic tweezers system. The vertical error bar indicates the standard error (se) of the mean value of the lifetime. 50–200 data points were obtained from at least five independent tethers at each force.

jumped to ~ 4 pN for 1 s to check whether the R7/KN complex was formed or not, since there is a distinct bead height difference between the paired and unpaired states of the molecule at ~ 4 pN (magenta data in Figure 2a). The force then jumped to the target force (e.g., ~ 7.2 pN, red data in Figure 2a) and kept at that force for sufficiently long time until the complete rupture of the R7/KN complex was observed. Figure 2a shows a representing time trace of the bead height recorded at ~ 7.2 pN (four further time traces are shown in Figure S4 in the Supporting Information), where the looped state of the detector lasted for ~ 25 s until unlooping (indicated by the red arrow) after the force jumped to ~ 7.2 pN. During the ~ 25 s before the unlooping transition, reversible stepwise bead height changes of step sizes of ~ 15 nm (indicated by blue arrows) resulted from partial unfolding/refolding of the R7/KN complex.

Figure 2b shows the resulting force-dependent lifetime of the R7/KN complex (gray data points). At each force, 50–200 data points were obtained from at least five independent tethers. The data can be fitted with exponentially decaying function (see Figure S5), which determines the time constant (i.e., the average lifetime) at different forces (red circles). The data reveal that the R7/KN complex can last for seconds to minutes over a force range up to 10 pN, with the maximum lifetime occurring at ~ 6 pN. The nonmonotonic force-dependence of the mechanical lifetime of the R7/KN complex indicates a switch from a catch-bond behavior (lifetime increases as force increases) to a slip-bond behavior (lifetime decreases as force increases) at forces of ~ 6 pN. The possible causes of this catch-to-slip switch behavior are discussed in the Discussion section.

Membrane Tethering Promotes Force-Dependent KN Localization to FA Periphery. The mechanical stability of the R7/KN complex is expected to have a strong dependence on the pulling geometry. We reasoned that KANK proteins may enrich at locations of FAs where the mechanical stability of the talin–KANK association is maximized. To test whether shear-force geometry leading to stronger mechanical stability could be a potential mechanism contributing to the peripheral localization of KANK proteins at FAs,^{7,10} we examined whether the KN domain, which, by itself, localizes throughout the FA,^{7,10} would display a different localization if tethered to the plasma membrane imposing a pulling geometry on the interaction with talin. To achieve this, we fused a membrane anchoring CAAX-motif of Ras GTPase to the C-terminus of the KN domain (Figure 3a). To exclude the potential effects of endogenous KANKs on the localization of KANK fragments, we used HeLa cells that were knocked out for KANK2 and depleted of KANK1, the two predominant KANK isoforms in these cells⁸ (see Figures S6a and S6b in the Supporting Information). Interestingly, the KN domain, either alone or with the adjacent “L1” linker region C-terminal of the KN domain (Figure 3a), localized throughout the FA, whereas the CAAX-fused version of KN-L1 was enriched at the periphery of FAs in a pattern that was reminiscent of the localization of the full-length KANK1 (see Figures 3b–d, as well as Figure S7 in the Supporting Information) in low expressing cells. In contrast, the L1-CAAX fusion without the KN domain was distributed evenly at the plasma membrane and showed no enrichment at FAs (see Figures 3c and 3d). The observed differences in the localization of KN-L1 and KN-L1-CAAX were unlikely to be due to the effects of these constructs on the FAs, as these constructs had no significant impact on the FA

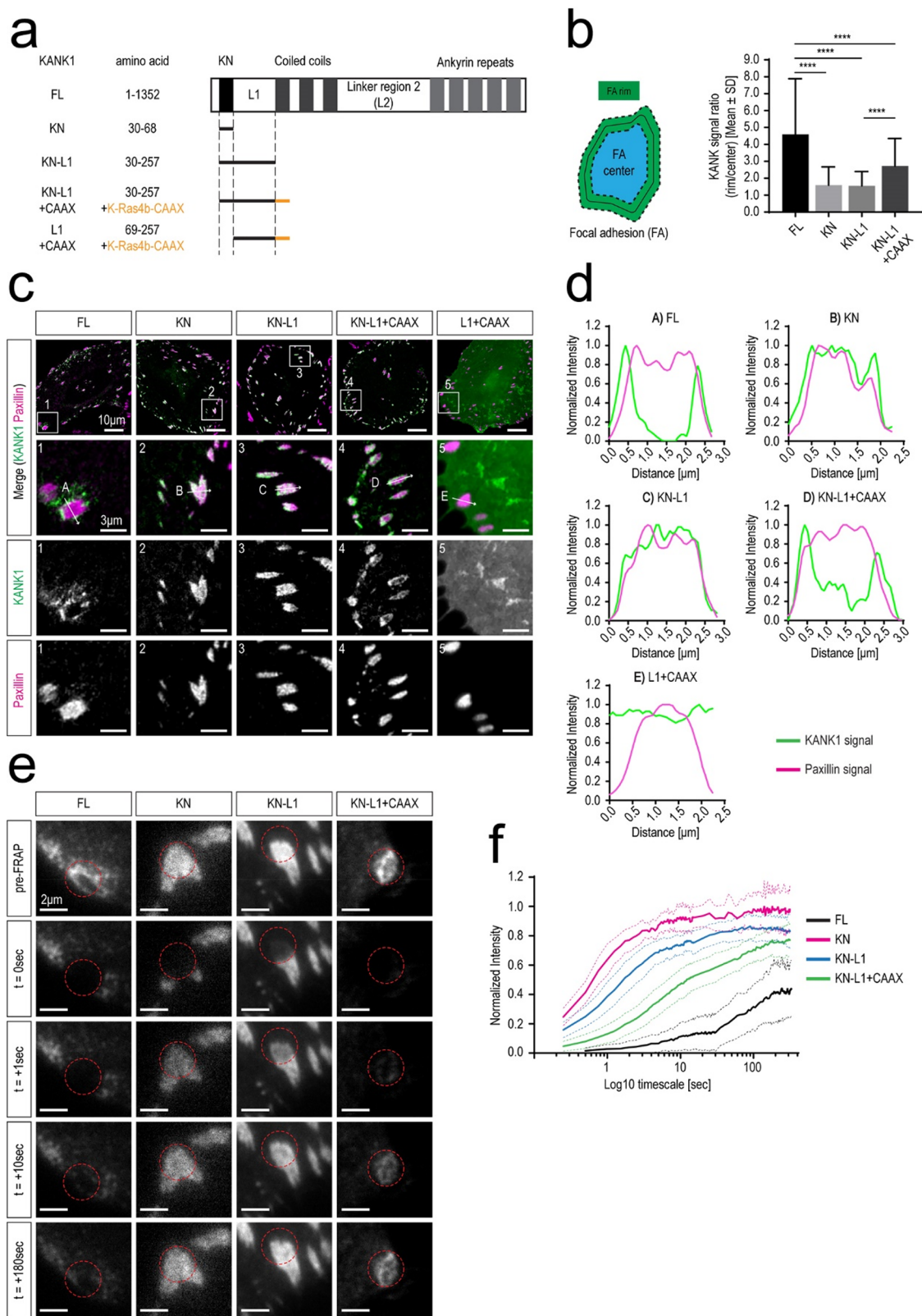


Figure 3. Localization of KANK1 and its KN-containing fragments at FAs. (a) Schematic representation of full-length KANK1 and the different KANK1 fragments. CAAX contains the membrane anchoring motif from K-Ras4b. (b) Quantification of KANK1 clustering at FAs. The left panel illustrates how the clustering of the different KANK1 constructs was analyzed: A ratio of the KANK1 signal at the FA rim, which extends 0.2 μ m beyond the FA outline and 0.2 μ m into the FA, to the KANK1 signal at the FA central part, was measured. The right panel shows the bar plot with the ratios expressed as mean \pm standard deviation. For each condition, 143–225 FAs were analyzed in at least two independent experiments (FL n = 145 [2 experiments]; KN n = 171 [3 experiments]; KN-L1 n = 143 [2 experiments], and KN-L1+CAAX n = 225 [2 experiments]). For statistical analysis, a one-way ANOVA test was performed using GraphPad Prism software (the horizontal lines denoted by the multiple asterisks symbol (***) denote statistical levels of $p < 0.0001$). (c, d) Localization of the indicated KANK1 constructs in HeLa cells. HeLa cells knockout for

Figure 3. continued

KANK2 and depleted of KANK1 using siRNA transfection were transiently transfected with GFP-tagged and siRNA-resistant KANK1 constructs (green). Cells were fixed and stained for the endogenous FA protein paxillin (magenta). Full-length KANK1 localizes exclusively to the FA rim (see enlargement 1 line scan in panel (c) and graph A in panel (d)) and is absent from the central area of FAs (see line scan in graph A in panel (d)). The KANK1-KN and the KANK1-KN-L1 constructs overlap with FAs and show high abundance in the central area of FAs (see enlargements 2 and 3 and line scans in panel (c) and graphs B and C in panel (d)). The addition of the membrane anchoring CAAX motif to the KANK1-KN-L1 construct (KANK1-KN-L1+CAAX) leads to enrichment in the FA rim area (see enlargement 4 and line scan in panel (c) and graph D in panel (d)). The membrane anchoring CAAX motif without the talin binding KN domain (KANK1-L1+CAAX) shows an even distribution at the plasma membrane and no enrichment at FAs (see enlargement 5 and line scan in graph E in panel (d)). The arrowed features labeled as “A”–“E” in panel (c) represent the direction of the line scans shown in panel (d). Three more line scans were performed for each of the 5 original line scans; the results are shown in Figure S7 in the Supporting Information. (e) Single frames of FRAP experiments in HeLa cells prepared as described above. A pre-FRAP image, the first frame after photobleaching ($t = 0$ s), and the indicated time points after FRAP of a 2.3- μm -diameter circle region in the KANK1 patch are shown. (f) Quantification of fluorescence recovery. The graph shows mean curves (bold lines) \pm standard deviation (light dotted lines) over time. For each condition, a total of 18–40 KANK1 patches were analyzed in two independent experiments (FL $n = 26$; KN $n = 18$; KN-L1 $n = 31$; KN-L1+CAAX $n = 40$).

number and the size (see Figure S6c). FRAP-based analysis of the turnover of different KN constructs showed that their localization reflected the part of the FA where they are preferentially recruited (throughout FA for KN or KN-L1, peripherally for KN-L1-CAAX) rather than some complex redistribution of the construct within FA after the binding (Figures 3e and 3f). These results are consistent with the hypothesis that plasma membrane tethering, which is expected to lead to a shear-force geometry of the talin–KANK1 interaction, can promote KANK1 enrichment at the FA periphery, possibly because the mechanical stability of KANK/talin association is maximized at these sites.

To investigate whether the peripheral distribution of KN-L1-CAAX is dependent on the pulling forces exerted on FAs, we attenuated these forces using the ROCK1 inhibitor Y27632, which induces gradual FA disassembly (see Figures S8a–S8d in the Supporting Information). Although the KN and KN-L1 fragments strongly colocalized with the FA marker paxillin at all time points, the KN-L1+CAAX fusion was located at the FA periphery but moved into the core of FA after the ROCK inhibitor treatment (Figure S8a). This was reflected by an increase in the correlation coefficient between the two signals (Figure S8b) and was also observed in live cells (Figure S8e). These data were similar to those obtained for full-length KANK1 in ROCK inhibitor-treated cells (Figure S8a–S8f), although full-length KANK1 never showed such a complete overlap with FA markers as the different KN fusions, because it also partly colocalized with the liprin-containing cortical sites (Figures S8a–S8f). Our data support the idea that forces exerted on talin play an important role in the localization of plasma membrane-tethered KN domain to the periphery of FAs.

DISCUSSION

Using a novel single-molecule detector to study protein–protein interactions with magnetic tweezers, we have quantified the mechanical stability of the talin–KANK complex. We find that, under shear-force geometry, this complex can withstand forces of several piconewtons for seconds to minutes. This force range lies within the physiological force level in the talin-mediated force-transmission pathway measured using a single-molecule force sensor.^{15,21,23,38,39} The survival time scale over this force range is similar to the talin lifetime in FAs in living cells (tens of seconds), based on talin turnover rate measurements.^{25,26,40} Therefore, the R7/KN complex is able to support a mechanically stable connection between talin and KANK1.

Because of the highly conserved sequences of KN motifs among all four KANK family proteins, similar mechanical stability can be expected for the complexes formed between R7 and KN from different KANK proteins. Together, these results suggest that the R7-KN interaction is capable of mediating a robust crosstalk between the actomyosin network and MTs at FAs. The functional implications of this cross-talk deserve further exploration. For example, a recent paper reported that depletion of either KANK1 or KANK2 or overexpression of the KN domain led to FA enlargement,¹¹ whereas we and others have observed no strong effects of KANK loss or KN expression on FA size or disassembly.^{7,10} Whether this reflects the distinct cell types used or other experimental differences requires further investigation.

An important finding is that the R7/KN complex has a maximum lifetime at forces of ~ 6 pN, indicating a catch-bond kinetics at forces below 6 pN. The catch-bond kinetics refers to an anti-intuitive phenomenon where the molecular lifetime increases as the force applied to the interacting molecules increases, which is often observed at a physiological level of forces^{41–43} under shear-force geometry.^{27,28,44} At forces above 6 pN, the R7/KN complex follows a slip-bond kinetics, which refers to quicker molecular dissociation at increased forces. Together, the R7/KN complex exhibits catch-to-slip switching behavior, which has an apparent advantage to define an optimal force range for stable talin/KANK connection.

As suggested in previous theoretical studies, such catch-to-slip switch behavior can be explained by multidimension models such as single-state multipathway models where the transitions starting from the same native state can follow different pathways, and multistate models where the transitions can start from different force-dependent competitive “native” states, each following a single pathway leading to unfolding/rupturing,^{45–49} or by differential entropic elastic extension fluctuation of the molecule in the native and the transition states at low forces (typically a few piconewtons), where the entropic elastic extension fluctuation cannot be ignored.^{27,28,50} Since the unlooping transition of the R7/KN detector could occur in two steps or one step at forces on the level of a few piconewtons, all these mechanisms are eligible candidates for the observed catch-to-slip switch behavior in our experiments.

Interestingly, we observed that the R7/KN complex can undergo partial unfolding before complete dissociation. Since KN is a single peptide in the R7/KN complex, the intrinsically disordered FH1 cannot contribute to unfolding signals,³² and the two I27 domains have an ultraslow unfolding rate at forces below 20 pN ($<0.001/\text{s}$ per domain),²⁷ this partial unfolding

should occur via the unraveling of a few α -helices in R7. The R7 domain contains five α -helices (H1–H5) and, based on the step size (~ 15 nm) of the partial unfolding and the corresponding unfolding force, we estimated that, under these conditions, approximately three α -helices should be unraveled from R7 and released under force. A previous molecular docking study suggested that the KN peptide mainly interacts with helices H2 and H5 in R7 (Figure 1a).⁷ Since the force is applied to the C-termini of KN and H5 of R7, according to the structure predicted based on molecular docking, one must assume that H5 needs to dissociate from KN. The step size of 15 nm observed for the partial unfolding suggests that H4 and H3 are likely also unraveled from R7. Based on this model, in the partially unfolded R7/KN complex, the KN peptide could remain bound to the H1/H2 coiled coil through the predicted interaction with H2 and potential interacting sites on the exposed H1 (Figure 1a, right (bottom panel)).

The mechanical stability of the R7/KN complex is expected to have a strong dependence on the pulling geometry. In this work, we quantified the mechanical stability of the R7/KN under the shear-force geometry, which provides the highest mechanical stability. We reason that this pulling geometry may play the most important role in mediating the stable connection between actomyosin network and CMSCs, since the R7/KN complexes formed under a less-stable pulling geometry may dissociate quickly. One could imagine that KANK proteins are likely enriched at locations under optimal pulling geometry (shear-force geometry) and optimal force range (~ 6 pN).

Interestingly, KANK proteins are enriched at the periphery of FAs.^{7,10} It remains unclear whether this localization can be explained by the mechanical stability of the talin–KANK complex, or whether it requires interactions between KANKs, talin, and other proteins. It is thought that competition between the KN domain and actin is a factor that contributes to the exclusion of KANKs from the FA cores.^{5,7} However, this mechanism is not sufficient to explain the peripheral enrichment of KANK at FAs, because the KN domain alone binds to talin throughout a focal adhesion (see, e.g., Figure 3). Experiments in cells have revealed that KANK1-KN-L1-CAAX preferentially localized to the periphery of FAs in low-expressing cells, while KANK1-KN and KANK1-KN-L1 without the CAAX motif were distributed more evenly throughout FAs, and the KANK1-L1-CAAX without the KN domain resulted in complete loss of the FA localization. Since the KANK1-KN-L1-CAAX construct lacks the domains interacting with any known KANK1 partners except talin, these results are consistent with the idea that the KN domain directs the FA localization of KANK and that the membrane tethering creates a shear-force geometry, which promotes KANK enrichment at FA periphery by increasing the mechanical stability of the talin–KANK linkage. Further support for the importance of forces exerted on the talin–KANK linkage for KANK localization is provided by the experiments on ROCK inhibition, which show that both full-length KANK1 and the membrane-tethered KN domain redistribute into the FA core when actomyosin contractility is attenuated. It will be interesting to measure the forces in talin molecules at different locations in FAs, which may provide additional insights into whether the optimal mechanical stability is a mechanism underlying the distribution of KANK proteins at FAs.

The single-molecule detector approach described in this study provides a highly effective way to directly quantify the mechanical stability of binary molecular complexes formed by two proteins or between two domains within one protein. In the future, applications of this approach will allow quantification of the mechanical stability of several crucial connections involved in various mechanotransduction pathways at different types of cell–ECM and cell–cell adhesions.

■ MATERIALS AND METHODS

Single-Protein Manipulation and Analysis. All *in vitro* single-protein stretching experiments were performed using a vertical magnetic tweezers setup.^{30,31} The channel is combined with a disturbance-free, rapid solution-exchange method⁵¹ to avoid flow-drag during sample preparation. Experiments were performed in solution containing 1X PBS, 1% BSA, 2 mM DTT, and 10 mM sodium L-ascorbate at 21 ± 1 °C. In typical magnetic tweezers experiments, the height of the super-paramagnetic bead from the bottom coverslip surface is recorded. The bead-height change is the extension change of the molecule when the force applied to the bead remains constant. When the force applied to the bead changes, the bead-height change is a combined effect of the force-dependent elastic extension change of the molecule and bead-rotation due to force-change-induced torque rebalance.^{33,52} Therefore, a concurrent stepwise bead-height change is usually observed during force jump (which takes ≤ 0.25 s in our setup). On the other hand, during the linear force-increase/force-decrease scans with a loading rate of ~ 0.5 – 1 pN s^{-1} used in our study, the stepwise bead-height change is the same as the stepwise extension change of the molecule. This is because the force change over the time window of the stepwise transition (≤ 0.01 s, the temporal resolution of our setup) is negligible (≤ 0.01 pN). More details of plasmid constructs, protein expression, and data analysis can be found in [Supplementary Text S1 and S2](#) in the Supporting Information.

Cell Culture and Transfection. HeLa cells knocked out for KANK2 were cultured in a DMEM medium with 10% (v/v) fetal calf serum and with 1% (v/v) penicillin/streptomycin. The cell line was routinely checked for mycoplasma contamination using Mycoalert assay (LT07–318, Lonza), following the supplier's instructions. Transfection of DNA and siRNA into these cells was performed as previously described in the work reported by van der Vaart et al.⁸ siRNAs were transfected using HiPerFect (Qiagen) at a concentration of 20 nM and cells were analyzed 72 h after transfection. DNA constructs were transfected using FuGene6 (Promega). More details of antibodies and immunofluorescence staining, DNA constructs and siRNAs, transfection procedures, generation of HeLa KANK2 knockout cell line, fluorescence microscopy and analysis, and fluorescence recovery after photobleaching and data analysis can be found in [Supplementary Text S3–S9](#) in the Supporting Information.

■ ASSOCIATED CONTENT

📄 Supporting Information

The Supporting Information is available free of charge on the [ACS Publications website](#) at DOI: [10.1021/acs.nanolett.9b01732](https://doi.org/10.1021/acs.nanolett.9b01732).

Figures describing the representative single-step unlooping events of the R7/KN complex during force-increase

scan (Figure S1); the partial unfolding and complete rupture force distribution of the R7/KN complex, as well as the corresponding Bell's model fittings of the distributions (Figure S2); unfolding force distribution of the R7 domain, as well as the corresponding Bell's model fittings of the distributions (Figure S3); representative time-bead height traces of complete rupture of the R7/KN complex (Figure S4); force-dependent lifetime distributions of R7/KN complex and the corresponding exponential decay fittings at different forces (Figure S5); FA size and number in cells transfected with different KANK1 constructs (Figure S6); the localization of KANK1 and its KN-containing fragments at FAs with three additional line scans at different angles (Figure S7); and the effects of ROCK inhibition on the localization of KANK at the focal adhesion rim (Figure S9). Supplementary texts include more details of plasmid constructs, protein expression, and data analysis of single molecule manipulation (Supplementary Text S1 and S2), and more details of antibodies and immunofluorescence staining, DNA constructs and siRNAs, transfection procedures, generation of HeLa KANK2 knockout cell line, fluorescence microscopy and analysis, and fluorescence recovery after photobleaching and data analysis (Supplementary Text S3–S9) (PDF)

AUTHOR INFORMATION

Corresponding Authors

*E-mail: a.akhmanova@uu.nl (A. Akhmanova).

*E-mail: phyjy@nus.edu.sg (J. Yan).

ORCID

Benjamin T. Goult: 0000-0002-3438-2807

Jie Yan: 0000-0002-8555-7291

Author Contributions

[#]These authors contributed equally to this work.

Author Contributions

J.Y., M.Y., and S.L. designed the study. M.Y. and S.L. performed the single-molecule stretching experiments and analyzed the data; Y.-C.A. and A.A. designed and performed the cell imaging experiments and data analysis. J.Y., M.Y., S.L., Y.-C.A., B.T.G., and A.A. interpreted the data. J.Y., M.Y., and S.L. wrote the paper. J.Y. and A.A. supervised the study.

Notes

The authors declare that all data supporting the findings of this study are available within the article and its Supporting Information, or they can be obtained from the corresponding author upon reasonable request.

The authors declare no competing financial interest.

ACKNOWLEDGMENTS

The authors thank Ms. Hongying Chen (protein cloning expression core, MBI) for her help on the protein expression, Dr. Diego Pitta de Araujo (science communication core, MBI) for his help on the illustrations. The research is funded by the Human Frontier Science Program (No. RGP00001/2016 to A.A., B.G., and J.Y.), and National Research Foundation, Prime Minister's Office, Singapore, under its NRF Investigatorship Programme (NRF Investigatorship Award No. NRF-NRFI2016-03, to J.Y.), and Singapore Ministry of Education Academic Research Fund Tier 3 (MOE2016-T3-1-002 to J.Y.,

in part). Y.-C.A. is supported by the Marie Skłodowska-Curie Actions Innovative Training Network (ITN) 675407 PolarNet.

REFERENCES

- (1) Arnaout, M. A.; Goodman, S. L.; Xiong, J. P. *Curr. Opin. Cell Biol.* **2007**, *19* (5), 495–507.
- (2) Elosgui-Artola, A.; Oria, R.; Chen, Y.; Kosmalska, A.; Perez-Gonzalez, C.; Castro, N.; Zhu, C.; Trepatt, X.; Roca-Cusachs, P. *Nat. Cell Biol.* **2016**, *18* (5), 540–8.
- (3) Kanchanawong, P.; Shtengel, G.; Pasapera, A. M.; Ramko, E. B.; Davidson, M. W.; Hess, H. F.; Waterman, C. M. *Nature* **2010**, *468* (7323), 580–4.
- (4) Fletcher, D. A.; Mullins, R. D. *Nature* **2010**, *463* (7280), 485–92.
- (5) Chen, N. P.; Sun, Z.; Fassler, R. *Curr. Opin. Cell Biol.* **2018**, *54*, 130–136.
- (6) Kakinuma, N.; Zhu, Y.; Wang, Y.; Roy, B. C.; Kiyama, R. *Cell. Mol. Life Sci.* **2009**, *66* (16), 2651–9.
- (7) Bouchet, B. P.; Gough, R. E.; Ammon, Y. C.; van de Willige, D.; Post, H.; Jacquemet, G.; Altelaar, A. M.; Heck, A. J.; Goult, B. T.; Akhmanova, A. *eLife* **2016**, *5*. DOI: 10.7554/eLife.18124.
- (8) van der Vaart, B.; van Riel, W. E.; Doodhi, H.; Kevenaer, J. T.; Katrukha, E. A.; Gumy, L.; Bouchet, B. P.; Grigoriev, I.; Spangler, S. A.; Yu, K. L.; Wulf, P. S.; Wu, J.; Lansbergen, G.; van Battum, E. Y.; Pasterkamp, R. J.; Mimori-Kiyosue, Y.; Demmers, J.; Olieric, N.; Maly, I. V.; Hoogenraad, C. C.; Akhmanova, A. *Dev. Cell* **2013**, *27* (2), 145–160.
- (9) Guo, Q.; Liao, S.; Zhu, Z.; Li, Y.; Li, F.; Xu, C. *J. Biol. Chem.* **2018**, *293* (2), 557–566.
- (10) Sun, Z.; Tseng, H. Y.; Tan, S.; Senger, F.; Kurzawa, L.; Dedden, D.; Mizuno, N.; Wasik, A. A.; Thery, M.; Dunn, A. R.; Fassler, R. *Nat. Cell Biol.* **2016**, *18* (9), 941–53.
- (11) Rafiq, N. B. M.; Nishimura, Y.; Plotnikov, S. V.; Thiagarajan, V.; Zhang, Z.; Shi, S.; Natarajan, M.; Viasnoff, V.; Kanchanawong, P.; Jones, G. E.; Bershadsky, A. D. *Nat. Mater.* **2019**, *18* (6), 638–649.
- (12) Goult, B. T.; Zacharchenko, T.; Bate, N.; Tsang, R.; Hey, F.; Gingras, A. R.; Elliott, P. R.; Roberts, G. C.; Ballestrem, C.; Critchley, D. R.; Barsukov, I. L. *J. Biol. Chem.* **2013**, *288* (12), 8238–49.
- (13) Gingras, A. R.; Bate, N.; Goult, B. T.; Hazelwood, L.; Canestrelli, I.; Grossmann, J. G.; Liu, H.; Putz, N. S.; Roberts, G. C.; Volkmann, N.; Hanein, D.; Barsukov, I. L.; Critchley, D. R. *EMBO J.* **2008**, *27* (2), 458–69.
- (14) Atherton, P.; Stutchbury, B.; Wang, D. Y.; Jethwa, D.; Tsang, R.; Meiler-Rodriguez, E.; Wang, P.; Bate, N.; Zent, R.; Barsukov, I. L.; Goult, B. T.; Critchley, D. R.; Ballestrem, C. *Nat. Commun.* **2015**, *6*, 10038.
- (15) Kumar, A.; Ouyang, M.; Van den Dries, K.; McGhee, E. J.; Tanaka, K.; Anderson, M. D.; Groisman, A.; Goult, B. T.; Anderson, K. I.; Schwartz, M. A. *J. Cell Biol.* **2016**, *213* (3), 371–83.
- (16) Hemmings, L.; Rees, D. J.; Ohanian, V.; Bolton, S. J.; Gilmore, A. P.; Patel, B.; Priddle, H.; Trevithick, J. E.; Hynes, R. O.; Critchley, D. R. *J. Cell Sci.* **1996**, *109* (Pt 11), 2715–2726.
- (17) Alam, T.; Alazmi, M.; Gao, X.; Arold, S. T. *Biochem. J.* **2014**, *460* (3), 317–29.
- (18) Goult, B. T.; Yan, J.; Schwartz, M. A. *J. Cell Biol.* **2018**, *217*, 3776–3784.
- (19) Margadant, F.; Chew, L. L.; Hu, X.; Yu, H.; Bate, N.; Zhang, X.; Sheetz, M. *PLoS Biol.* **2011**, *9* (12), No. e1001223.
- (20) Yan, J.; Yao, M.; Goult, B. T.; Sheetz, M. P. *Cell. Mol. Bioeng.* **2015**, *8* (1), 151–159.
- (21) Grashoff, C.; Hoffman, B. D.; Brenner, M. D.; Zhou, R.; Parsons, M.; Yang, M. T.; McLean, M. A.; Sligar, S. G.; Chen, C. S.; Ha, T.; Schwartz, M. A. *Nature* **2010**, *466* (7303), 263–6.
- (22) Austen, K.; Ringer, P.; Mehlich, A.; Chrosteck-Grashoff, A.; Kluger, C.; Klingner, C.; Sabass, B.; Zent, R.; Rief, M.; Grashoff, C. *Nat. Cell Biol.* **2015**, *17* (12), 1597–606.
- (23) Ringer, P.; Weissl, A.; Cost, A. L.; Freikamp, A.; Sabass, B.; Mehlich, A.; Tramier, M.; Rief, M.; Grashoff, C. *Nat. Methods* **2017**, *14* (11), 1090–1096.

- (24) Yao, M.; Goult, B. T.; Klapholz, B.; Hu, X.; Toseland, C. P.; Guo, Y.; Cong, P.; Sheetz, M. P.; Yan, J. *Nat. Commun.* **2016**, *7*, 11966.
- (25) Himmel, M.; Ritter, A.; Rothemund, S.; Pauling, B. V.; Rottner, K.; Gingras, A. R.; Ziegler, W. H. *J. Biol. Chem.* **2009**, *284* (20), 13832–13842.
- (26) Hakonarrottir, G. K.; Lopez-Ceballos, P.; Herrera-Reyes, A. D.; Das, R.; Coombs, D.; Tanentzapf, G. *Mol. Biol. Cell* **2015**, *26* (22), 4149–4162.
- (27) Yuan, G.; Le, S.; Yao, M.; Qian, H.; Zhou, X.; Yan, J.; Chen, H. *Angew. Chem., Int. Ed.* **2017**, *56* (20), 5490–5493.
- (28) Guo, S.; Tang, Q.; Yao, M.; You, H.; Le, S.; Chen, H.; Yan, J. *Chem. Sci.* **2018**, *9* (27), 5871–5882.
- (29) Wang, X.; Ha, T. *Science* **2013**, *340* (6135), 991–4.
- (30) Chen, H.; Fu, H.; Zhu, X.; Cong, P.; Nakamura, F.; Yan, J. *Biophys. J.* **2011**, *100* (2), 517–23.
- (31) Le, S.; Liu, R.; Lim, C. T.; Yan, J. *Methods* **2016**, *94*, 13–8.
- (32) Yu, M.; Le, S.; Efremov, A. K.; Zeng, X.; Bershadsky, A.; Yan, J. *Nano Lett.* **2018**, *18* (8), 5239–5247.
- (33) Zhao, X.; Zeng, X.; Lu, C.; Yan, J. *Nanotechnology* **2017**, *28* (41), 414002.
- (34) Bell, G. I. *Science* **1978**, *200* (4342), 618–27.
- (35) Le, S.; Yu, M.; Hovan, L.; Zhao, Z.; Ervasti, J.; Yan, J. *ACS Nano* **2018**, *12* (12), 12140–12148.
- (36) Marko, J. F.; Siggia, E. D. *Macromolecules* **1995**, *28* (26), 8759–8770.
- (37) Bustamante, C.; Marko, J. F.; Siggia, E. D.; Smith, S. *Science* **1994**, *265* (5178), 1599–600.
- (38) Morimatsu, M.; Mekhdjian, A. H.; Adhikari, A. S.; Dunn, A. R. *Nano Lett.* **2013**, *13* (9), 3985–9.
- (39) Roca-Cusachs, P.; Conte, V.; Trepast, X. *Nat. Cell Biol.* **2017**, *19* (7), 742–751.
- (40) Hernandez-Varas, P.; Berge, U.; Lock, J. G.; Stromblad, S. *Nat. Commun.* **2015**, *6*, 7524.
- (41) Huang, D. L.; Bax, N. A.; Buckley, C. D.; Weis, W. I.; Dunn, A. R. *Science* **2017**, *357* (6352), 703–706.
- (42) Sarangapani, K. K.; Qian, J.; Chen, W.; Zarnitsyna, V. I.; Mehta, P.; Yago, T.; McEver, R. P.; Zhu, C. *J. Biol. Chem.* **2011**, *286* (37), 32749–61.
- (43) Sokurenko, E. V.; Vogel, V.; Thomas, W. E. *Cell Host Microbe* **2008**, *4* (4), 314–23.
- (44) Marshall, B. T.; Long, M.; Piper, J. W.; Yago, T.; McEver, R. P.; Zhu, C. *Nature* **2003**, *423* (6936), 190–3.
- (45) Evans, E.; Leung, A.; Heinrich, V.; Zhu, C. *Proc. Natl. Acad. Sci. U. S. A.* **2004**, *101* (31), 11281–6.
- (46) Barsegov, V.; Thirumalai, D. *Proc. Natl. Acad. Sci. U. S. A.* **2005**, *102* (6), 1835–9.
- (47) Pierce, C. A.; Dudko, O. K. *Phys. Rev. Lett.* **2017**, *118* (8), 088101.
- (48) Pereverzev, Y. V.; Prezhdo, O. V.; Forero, M.; Sokurenko, E. V.; Thomas, W. E. *Biophys. J.* **2005**, *89* (3), 1446–54.
- (49) Bartolo, D.; Derenyi, I.; Ajdari, A. *Phys. Rev. E: Stat. Phys., Plasmas, Fluids, Relat. Interdiscip. Top.* **2002**, *65* (5), 051910.
- (50) Guo, S.; Efremov, A. K.; Yan, J. *Commun. Chem.* **2019**, *2* (1), 30.
- (51) Le, S.; Yao, M.; Chen, J.; Efremov, A. K.; Azimi, S.; Yan, J. *Nucleic Acids Res.* **2015**, *43* (17), No. e113.
- (52) Fu, H.; Le, S.; Chen, H.; Muniyappa, K.; Yan, J. *Nucleic Acids Res.* **2013**, *41* (2), 924–32.